SenScaffold: A 3D-Printed Porous Dielectric Resonator as a Self-Sensing Scaffold

Paris Sofokleous, Eva Paz, and Francisco Javier Herraiz-Martínez, *Member, IEEE*

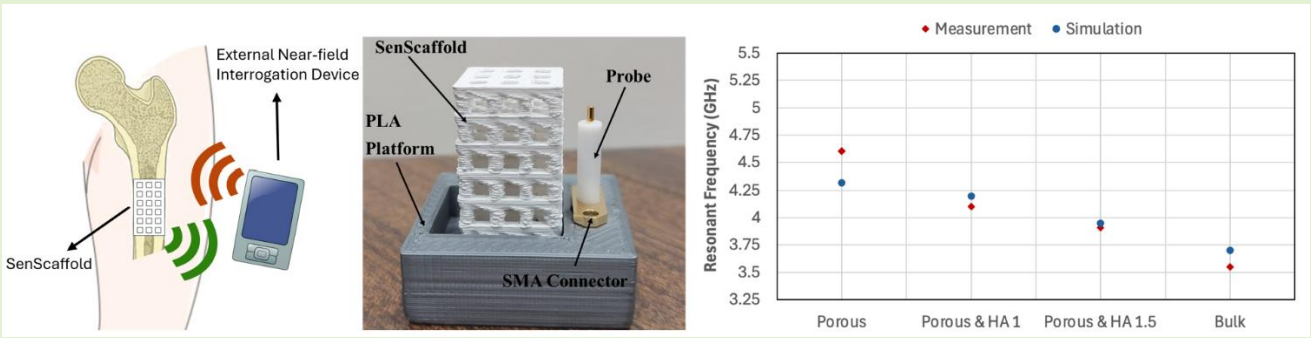

***Abstract*—This study presents a proof of concept for the design, fabrication, and characterization of a 3D-printed porous dielectric resonator (DR) scaffold for real-time, non-invasive monitoring of bone regeneration. A scaffold is a biocompatible, porous structure that supports cell attachment, growth, and tissue formation to heal large bone defects. Full-wave simulations confirm that the porous DR exhibits electromagnetic (EM) field distributions similar to a conventional rectangular DR, with a frequency shift due to its porosity. The self-sensing scaffold is fabricated via Fused Deposition Modeling (FDM) 3D printing using polylactic acid (PLA) reinforced with zirconia (PLA_ ZrO_2). It is then covered with one or more printed layers of PLA reinforced with hydroxyapatite (PLA_HA) to simulate varying stages of bone growth, as PLA_HA possesses a relative permittivity similar to that of natural bone. Theoretical and experimental results demonstrate that the resonant frequency shifts inversely with HA layer thickness, validating the scaffold's ability to function as a passive sensor for detecting and tracking tissue regeneration. A comparison of simulated and experimental field distributions confirms that the porous DR sustains a resonant mode suitable for interrogation via a coaxial probe coupled to the scaffold in the near-field region. Experimental evaluation reveals a high sensitivity of 500 MHz/mm during the initial stages of bone growth (up to 1 mm) and 380 MHz/mm for subsequent stages, confirming the system's capability for early-stage clinical monitoring. This work represents an initial step toward a clinically relevant monitoring system, demonstrating that porous DR scaffolds can act as functional biosensors with integrated self-sensing capabilities. The ability to monitor bone regeneration via EM interrogation offers a scalable, wireless, non-invasive approach for real-time biomedical diagnostics. A key advantage of self-sensing scaffold is that it functions itself as a sensor, eliminating the need for additional components or devices within the body. The same structure that supports bone regeneration also enables real-time monitoring.**

***Index Terms*—3D-printing, Additive Manufacturing (AM), Bone regeneration, Dielectric Resonator (DR), Electromagnetic (EM) biosensor, Scaffold.**

I. Introduction

THE increasing prevalence of bone health issues highlights the need for advanced surgical procedures and innovative bone graft alternatives. Implementing advanced bone-surgery procedures is essential for driving significant improvements in treating thousands of patients who require bone-scaffold grafts in the coming years [1]. A bone scaffold is a porous structure designed to support bone tissue regeneration by providing a framework for cell growth, attachment, and nutrient transport [2]. Developing new materials, fabrication techniques, and optimized scaffold designs offers a promising solution to address the limitations of traditional autografts and allografts, including donor-site morbidity, immune rejection, limited availability, and infection risk [3]. To address these challenges, synthetic bone implants, such as scaffolds, have become increasingly prevalent over the past few years. Several studies have investigated the development of bone tissue scaffolds using conventional fabrication techniques, such as solvent casting/particulate leaching, gas foaming, and phase separation [4]–[5].

Recent research studies have focused on developing personalized bone prosthetic materials that meet bone scaffolds'

Submitted: 22nd December 2025. Paris Sofokleous was the recipient of an "IIT Strategic PhD Research Grant" from Universidad Pontificia Comillas, which funded his doctoral research activities..

P. Sofokleous was with the Institute for Research in Technology (IIT), ICAI School of Engineering, Universidad Pontificia Comillas, Madrid, 28015 Spain (e-mail: psofokleous@comillas.edu).

E. Paz is with the Institute for Research in Technology (IIT), ICAI School of Engineering, Universidad Pontificia Comillas, Madrid, 28015 Spain (e-mail: epaz@iit.comillas.edu).

F. J. Herraiz-Martínez is with the Institute for Research in Technology (IIT), ICAI School of Engineering, Universidad Pontificia Comillas, Madrid, 28015 Spain (e-mail: fjherraiz@icai.comillas.edu).

regenerative and mechanical requirements by a controllable and precise manufacturing process, primarily due to advancements in 3D-printing technologies [6]−[8]. 3D printing, also known as additive manufacturing (AM), is a highly versatile fabrication technique capable of producing various materials, including polymers, ceramics, metals, and composites, with customized/complex shapes, tailored pore size/porosity, and high precision [9]. Moreover, it is emerging as a pivotal tool in biomedical/tissue engineering, supporting 3D cell culture within complex biomimetic structures [10] and contributing to the transformation and advancement of orthopedic surgery and medicine in general [11]. 3D printing demonstrates superior therapeutic efficacy [12] and enhanced material properties [13] for bone scaffolds development compared to conventional techniques, such as pore-forming agent leaching, gas foaming, and phase separation methods.

In this work, Fused Deposition Modeling (FDM), a material extrusion AM 3D-printing technology, is selected for scaffold fabrication. FDM offers precise control over scaffold geometry and porosity, enabling the fabrication of complex, patient-specific structures with reproducible pore architectures. In addition, its compatibility with polymer-ceramic composite filaments, scalability, and cost-effectiveness make it well-suited for prototyping and experimental validation of porous bone scaffolds [14]−[15].

Despite the advantages offered by artificial scaffolds in bone tissue engineering, one of the main challenges lies in extracting detailed information about their in vivo behaviour. Accurately obtaining comprehensive data about the current condition of bone grafts and the surrounding biological environment remains a significant obstacle in monitoring implants and scaffolds within the body. The most commonly employed methods today rely on X-ray imaging techniques, including radiography, computed tomography, and magnetic resonance imaging [16]−[17]. While these techniques offer some insight into the state of grafts and cellular evolution, they are limited in the level of detail provided and do not allow for continuous and cost-effective monitoring of the early stages of bone regeneration, particularly during the first critical days, which are decisive for proper scaffold integration and biological acceptance, when frequent imaging follow-up is neither practical nor feasible in clinical practice. Additionally, they pose potential health risks due to exposure to ionizing radiation. For this reason, a solution that enables simple, real-time, and non-invasive monitoring, especially during the first days when complications are most likely, would represent a major advance.

To address these limitations, microwave (MW) sensing has emerged as a non-invasive modality capable of monitoring bone graft scaffolds, tracking their progress, and detecting physiological events within the body. MW sensors are extensively employed in biomedical and industrial applications [18]−[19] due to their numerous advantages, including cost-effective implementation and operation, ease of use, and exceptional versatility. Reported works in the literature demonstrate high sensitivity under specific applications and conditions [20]. Additionally, electromagnetic (EM) signals utilized by MW sensors operate within a frequency range of hundreds of MHz to tens of GHz. This range falls within the non-ionizing radiation spectrum, making it inherently safe and posing no health risks [21].

Dielectric resonator (DR)-based sensors have evolved from conventional MW components into robust sensing platforms, primarily because their resonant characteristics exhibit high sensitivity to variations in permittivity and loss in the surrounding media [22]. This characteristic enables the realization of compact, passive sensing platforms in which variations in the target measurand are inferred from shifts in resonant frequency and/or quality factor, thereby enabling non-contact, wireless interrogation in applications where wired sensing is impractical. In mechanical sensing applications, DRs have been demonstrated as passive sensing elements capable of detecting force, torque, stress, and pressure by mechanically inducing perturbations in the resonant cavity, with changes in geometry (e.g., air-gap variation) leading to measurable shifts in resonant frequency [23]. In chemical sensing, DRs have been widely employed for dielectric characterization of liquids and mixtures, with changes in chemical composition [24]. Moreover, at MW frequencies, DRs have been shown to be sensitive to variations in the dielectric properties of biological media, enabling the monitoring of physiological or compositional changes in biological fluids and tissues via resonance perturbation [25].

In recent years, 3D-printed DRs have been used in telecommunication and sensing applications, attracting significant attention as filters [26], antennas [27], and oscillators [28] using commercially available, low-cost filaments. Most recently, DR-based passive wireless sensors have also been developed using a high relative permittivity (ε_r) dielectric material to respond to EM signals as a wireless passive sensor [29]−[30].

Among ceramic materials, zirconia (ZrO_2) and hydroxyapatite (HA), known for their biocompatibility and performance, have emerged as two potential candidates for biomedical and sensing applications. ZrO_2 is a promising material for designing dielectric resonators (DRs) due to its ε_r, making it particularly suitable for sensing applications as has been previously demonstrated [31]. On the other hand, HA has been extensively studied and widely used in biomedical applications due to its exceptional bioactivity and osteoconductive properties [32]−[33]. These materials present a unique opportunity to develop scaffolds that support bone regeneration while enabling non-invasive, real-time monitoring through EM interrogation. For this purpose, polylactic acid (PLA)-based materials incorporated with ZrO_2, and HA fillers were used in this study.

In addition, it should be emphasized that this work is intended as a proof-of-concept and focuses on the early stages of bone regeneration, where continuous monitoring is most critical. The complexity of incorporating realistic biological conditions will be addressed progressively in future studies.

This study aims to advance scaffold design by transforming conventional bone-prosthesis scaffolds into "self-sensing scaffolds", hereafter referred to as SenScaffolds. The proposed

approach establishes a proof-of-concept in which a porous DR simultaneously serves as a bone scaffold, preserving its mechanical and biological properties, and acting as a passive EM sensor. The SenScaffold is wirelessly interrogated using an external near-field probe, enabling non-invasive monitoring without embedded electronics. Bone regeneration is experimentally emulated by progressively introducing HA layers into the porous scaffold, and the corresponding regeneration stage is quantified through changes in the EM field response induced by the SenScaffold. This approach demonstrates the feasibility of integrating sensing functionality directly into the scaffold architecture for monitoring bone regeneration.

The rest of this paper is structured as follows. Section II presents the system setup used in this study, along with the current technology for interrogating porous SenScaffolds. Section III describes the 3D-printing technology and the fabrication process of the scaffolds, as well as the dielectric characterization of the materials used in this study. In Section IV, the modal analysis and full-wave simulations of the porous DR are discussed, comparing bulk and porous DR structures while illustrating the electric field distributions and assessing the feasibility of using porous DR. Section V details the sensing principle of the system, analyzing the resonant frequencies of the SenScaffolds with simulated HA layers for bone growth. This section also presents the full-wave simulations of the final setup. Section VI focuses on the experimental results, including the fabrication of the final prototypes and the sensing measurements, comparing simulated and experimental findings. Section VII provides a technical comparison between the proposed interrogation method and alternative detection techniques. Section VIII outlines future works and perspectives focused on further optimization and practical application of the proposed approach. Finally, Section IX presents the core conclusions of this study.

II. System Setup

A schematic illustration of the underlying principle of the SenScaffold concept, integrated into a large bone model, is shown in Fig. 1. A porous DR, designed as a SenScaffold, is introduced as a support for bone regeneration. The SenScaffold is engineered to respond to changes in its surrounding environment, modifying its EM response as a function of bone growth. This property enables it to serve as both a structural support for bone regeneration and a functional wireless sensor without requiring additional electronic components inside the body. The SenScaffold is fabricated using 3D-printing technology to have a high control of the geometry and porosity. To interrogate the SenScaffold wirelessly, a near-field antenna probe is positioned in close proximity, outside of the body, transmitting MW signals and detecting the scaffold's EM response.

This setup aims to establish the foundational conditions necessary for validating the self-sensing principle of the scaffold, particularly for applications in real-time, non-invasive bone regeneration monitoring. The near-field antenna will be optimized for effective signal transmission and reception, ensuring accurate measurement of scaffold interactions. By leveraging this system, the study explores the potential of EM-based sensing technology for real-time, non-invasive assessment of scaffold performance in biomedical applications.

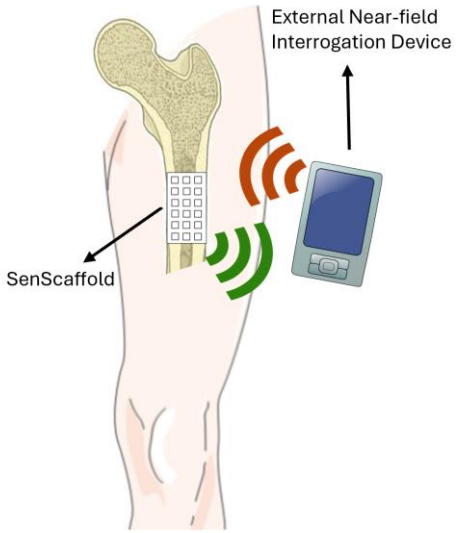

Fig. 1. Schematic illustration of the SenScaffold interrogation setup for wireless bone regeneration monitoring, integrated into a bone model.

III. 3D Printing Process & Dielectric Characterization

In this study, polymeric filaments and pellets reinforced with ceramic fillers, were selected to develop the SenScaffolds due to their unique combination of biological compatibility, dielectric properties, and suitability for AM. Specifically, a composite filament of PLA with 50% ZrO_2 as a filler (PLA_ZrO_2), and PLA pellets reinforced with 50% HA (PLA_HA), were chosen for this work. These materials meet the biological requirements for scaffold development while offering high relative permittivity, which is essential for effective EM sensing. The PLA_ZrO_2 composite used in this study has been previously characterized by the authors in terms of both dielectric and mechanical properties [31], as part of the evaluation of ceramic-polymer systems suitable for AM. In this work, mechanical performance was not considered a primary selection criterion, as the required properties depend on the anatomical location and clinical application. The focus here is to establish the EM design requirements of the SenScaffold and validate its sensing capability. Once defined, alternative material formulations can be considered to preserve the required dielectric properties while optimizing mechanical and biological performance in future developments.

Moreover, the use of 3D-printing technology is crucial in this context, as it enables the fabrication of complex porous structures with high precision - an essential factor for ensuring the scaffold's functionality. FDM was selected as a cost-effective and accessible method for producing these scaffolds while maintaining the accuracy required for the porous design.

Given these advantages, the combination of ceramic-reinforced polymeric materials and 3D-printing technology provides an optimal solution for developing SenScaffolds with tailored EM and biological properties. A commercial FDM 3D printer (TUMaker Dual Pro) was used to manufacture the scaffolds in this study.

First, a slicer software (Simplify) was used to adjust printing parameters for each material, including printing and bed temperatures, print speed, layer height, nozzle diameter, etc. Scaffold prototypes and bricks for the dielectric characterization of the materials were all printed with 100% infill density without any post-curing process. The program enables the conversion of 3D model files in .stl file format into the G-code programming language for the 3D printer. Before printing, it was necessary to find the optimal parameters for each material. This is especially relevant for ceramic-polymer materials, which present significant challenges in printing due to their inherent brittleness and the tendency to form agglomerates. Table I shows the optimized printing parameters used in each case.

TABLE I
MAIN PRINTING PARAMETERS OF THE MATERIALS UNDER STUDY

Parameter	PLA_ZrO_2	PLA_HA
Printing Temperature	180ºC	170ºC
Bed Temperature	45ºC	45ºC
Infill	100%	100%
Layer height	0.2 mm	0.2 mm
Printing speed	30mm/s	25mm/s
Cooling	ON	ON
Nozzle diameter	0.6	0.6

The printing parameters were selected to ensure reliable fabrication, dimensional accuracy, and material consistency of the SenScaffold prototypes. A 100% infill density was adopted to produce fully solid structures, which is required to obtain representative dielectric properties and to ensure that the fabricated scaffolds accurately reflect the intended bulk material behavior, while also improving structural integrity and repeatability across prototypes. The extrusion temperature was set within the recommended melting ranges of the filament and pellet materials to promote uniform material flow and strong interlayer adhesion, particularly important for printing ceramic-polymer composites. To further enhance printability and prevent nozzle clogging caused by material agglomeration, relatively low and stable processing temperatures were combined with a reduced printing speed. The selected layer height corresponds to the resolution limits of the employed FDM process, providing a balance between printing accuracy and fabrication stability. Active cooling was enabled to stabilize the deposited layers and mitigate geometric deformation during printing, especially in regions with fine features. Finally, the nozzle diameter was selected to ensure consistent extrusion and material compatibility. While these parameters were optimized to achieve the best possible precision and repeatability, 3D printing with high-loaded ceramic-polymer composites remains a complex process. The inherent brittleness of these materials and the potential for micro-agglomerates during extrusion inevitably result in dimensional tolerances, which are further evaluated in subsequent Sections.

For the dielectric characterization, a Split Post Dielectric Resonator (SPDR) from QWED [34] connected to a Vector Network Analyzer (VNA) Anritsu MS46122B [35] was used for measuring the relative permittivity (ε_r), and the loss tangent (tan δ) of laminar dielectric 3D-printed brick materials with dimensions of 60 mm × 100 mm × 2 mm (length × width × height). The terms length and width refer to the in-plane dimensions of the samples (x and y direction, respectively), while height corresponds to the dimension along the printing (z) direction. SPDR functions as a resonant cavity with a slot for sample insertion [34]. Following established protocols, the resonant frequency and Q factor of each transmission measurement ($|S_{21}|$) for both the empty cavity and the cavity containing the sample under study. Based on these parameters and the height of each 3D-printed brick, the ε_r and tan δ of each sample were determined. This characterization follows a standardized and proven procedure for ceramic-polymer composite filaments, as previously detailed and validated by the authors in [31]. The characterization results for the PLA_ZrO_2 filament were ε_r = 7.45 and tan δ = 0.0078, while for the PLA_HA pellets, the values were ε_r = 4.46 and tan δ = 0.0329.

IV. MODAL ANALYSIS & POROUS DIELECTRIC RESONATOR

A. Modal Analysis of the Rectangular Bulk DR

First, a bulk rectangular DR is considered for modal analysis. This serves as a reference for comparison with the porous DR introduced later in the study. The main views of the rectangular bulk DR, including its dimensional parameters, are shown in Fig. 2(a). The rectangular bulk DR is a solid dielectric block with a relative permittivity ε_r and dimensions L_x, L_y, and L_z.

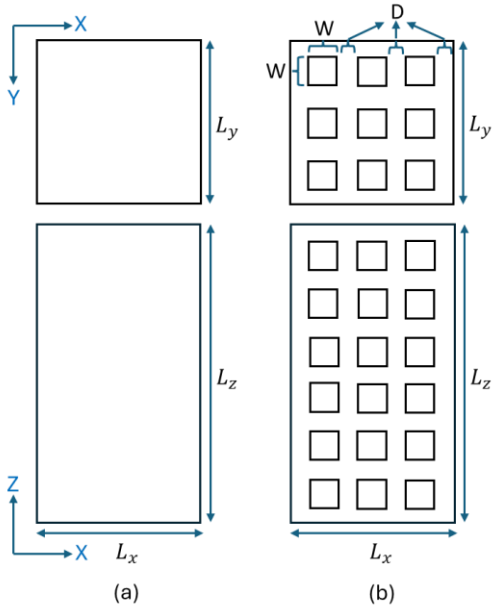

Fig. 2. Bulk (a) and Porous (b) DR scaffolds with their respective geometric parameters, pore dimensions, and inter-pore spacing.

Since the permittivity of the dielectric is significantly higher than that of air, the dielectric-air interface can be approximated as a Perfect Magnetic Conductor (PMC). Then, all the boundary conditions are PMC [36]. This translates into the following wave function:

$$\psi_z = X(x)\,Y(y)\,Z(z) = (\mathrm{A}_1 \sin_{\mathrm{x}}\mathrm{x} + \mathrm{A}_2 \cos_{\mathrm{x}}\mathrm{x})\,(\mathrm{A}_3 \sin_{\mathrm{y}}\mathrm{y} + \mathrm{A}_4 \cos_{\mathrm{y}}\mathrm{y})\,(\mathrm{A}_5 \sin_{\mathrm{z}}\mathrm{z} + \mathrm{A}_6 \cos_{\mathrm{z}}\mathrm{z}) \quad (1)$$

Both transversal magnetic (TM) and transversal electric (TE) modes are supported by the rectangular DR. In both cases, applying the PMC boundary conditions gives the following eigenvalues:

$$k_x = \frac{m\pi}{L_x} \quad (2)$$

$$k_y = \frac{n\pi}{L_y} \quad (3)$$

$$k_z = \frac{p\pi}{L_z} \quad (4)$$

In the case of the TM modes *m* and *n* can take values 0,1,2,3... whereas *p* can take values 1, 2, 3, … except *m*=*n*=0 which is not allowed. For the TE modes *m* and *n* can take values 1,2,3... whereas *p* can take values 0, 1, 2, 3, … In both cases the resonant frequency of each mode is calculated from [37]:

$$(f_r)m,n,p = \frac{c}{2\pi\sqrt{\varepsilon_r}}\sqrt{(\frac{m\pi}{L_x})^2 + (\frac{n\pi}{L_y})^2 + (\frac{p\pi}{L_z})^2} \quad (5)$$

Where *c* is the speed of light in vacuum.

Considering $L_z > L_x, L_y$, the fundamental mode is TM_{101} or TM_{011}. In this study we will consider a square base DR. Thus, $L_x = L_y$ and the modes TM_{101} and TM_{011} are degenerated. Taking TM_{101} as a reference, (5) simplifies to:

$$f_{101} = \frac{c}{2\sqrt{\varepsilon_r}}\sqrt{\frac{1}{{L_x}^2} + \frac{1}{{L_z}^2}} \quad (6)$$

Considering that $H_z = 0$ and $E_z \neq 0$ in the TM modes, applying the PMC boundary conditions and substituting the indices values $(m = 1, n = 0, p = 1)$, the TM_{101} present the following electric field [38]:

$$E_x = \frac{k_x k_z}{k_{mnp}^2 - k_z^2} E_0 sin\left(\frac{\pi x}{L_x}\right) cos\left(\frac{\pi z}{L_z}\right) \quad (7)$$

$$E_y = 0 \quad (8)$$

$$E_z = E_0 cos\left(\frac{\pi x}{L_x}\right) sin\left(\frac{\pi z}{L_z}\right) \quad (9)$$

Where E_0 constant is determined by the excitation and boundary condition.

From the previous derivation and considering the expression for E_z, we can obtain the following magnetic field for the fundamental mode [38]:

$$H_x = 0 \quad (10)$$

$$H_y = -\frac{i\omega_{mnp}\varepsilon k_x}{k_{mnp}^2 - k_z^2} E_0 sin\left(\frac{\pi x}{L_x}\right) sin\left(\frac{\pi z}{L_z}\right) \quad (11)$$

$$H_z = 0 \quad (12)$$

The proposed design is made of PLA reinforced with ZrO_2, whose dielectric properties are reported in Section III. To justify the simulation results with theory, the resonant frequency of the TM_{101} mode was calculated using the analytical formula and compared with the simulated value. The resonant frequency of the TM_{101} mode in a rectangular resonator can be calculated using (6). The proposed dimensions for the resonator are $L_x = L_y = 17\ mm$ and $L_z = 32\ mm$. Substituting the values of the proposed design, where $c \approx 3 \times 10^8\ m/s$, the value of the theoretical resonant frequency is 3.66 GHz. This proposed solid resonator was simulated with the eigenmode solver of CST Studio Suite [39]. The computed fundamental frequencies match the ones obtained by theory.

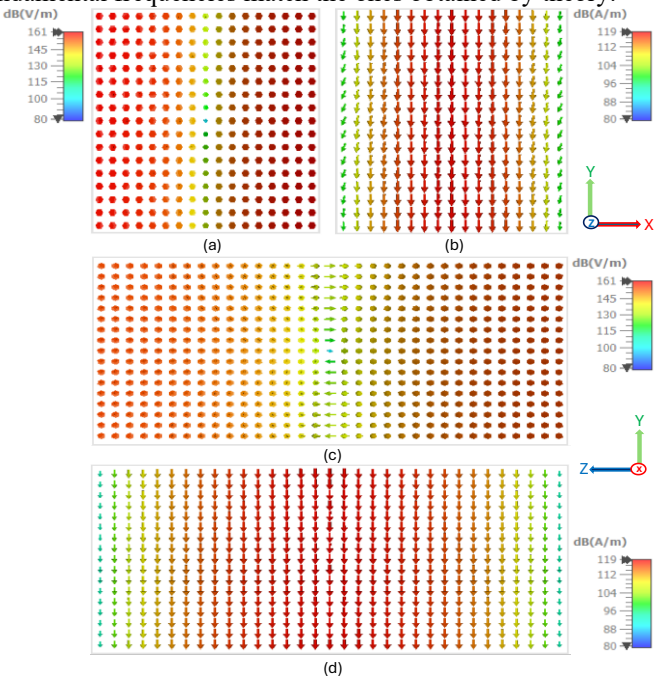

Fig. 3. Simulated electric (a, c) and magnetic (b, d) field distributions of the fundamental TM_{101} mode for the bulk DR. Top views are shown in (a, b) and side views in (c, d).

Selected views of the simulated electric and magnetic field distributions corresponding to the fundamental mode of the rectangular bulk DR are shown in Fig. 3. The longitudinal magnetic field component, $\mathrm{H_z}$, is 0. These distributions are consistent with equations (7) – (12), and they confirm that the mode excited within the bulk resonator is the fundamental TM_{101} mode.

This article has been accepted for publication in IEEE Sensors Journal. This is the author's version which has not been fully edited and
content may change prior to final publication. Citation information: DOI 10.1109/JSEN.2026.3677655

In the simulation, the resonant frequency of the TM_{101} mode was found to be 3.66 GHz, which perfectly matches the theoretical value, confirming the accuracy of the simulation setup and the validity of the observed mode as TM_{101}.

B. Porous Dielectric Resonator

To quantitatively assess the influence of porosity on the resonant behavior, a rectangular porous scaffold was designed and analyzed. This structure introduces porosity into the DR to adapt it for use as a bone scaffold, while maintaining the same overall dimensions as the bulk resonator. A periodic porosity pattern was implemented, consisting of 6 × 3 pores on the lateral surfaces and 3 × 3 pores on the top surface, as illustrated in Fig. 2(b).

The presence of porosity modifies the EM properties of the structure, as the air-filled pores change the effective permittivity (ε_{eff}) of the scaffold, and therefore the resonant frequency of the scaffold. The level of porosity significantly impacts the mechanical properties of scaffolds as well. A high level of porosity enhances the delivery of nutrients and oxygen and enables cell growth. However, excessive porosity can lead to structural weaknesses.

To calculate the frequency of the porous scaffold, the modified (6) becomes:

$$f_{101} = \frac{c}{2\sqrt{\varepsilon_{eff}}}\sqrt{\frac{1}{{L_x}^2} + \frac{1}{{L_z}^2}} \tag{13}$$

Where ε_{eff} is a weighted average of the permittivity of air and ZrO_2. This can be quantified using the formula:

$$\varepsilon_{eff} = (1-\varphi)\varepsilon_r + \varphi\varepsilon_{vacuum} \tag{14}$$

φ is the porosity, given by:

$$\varphi = \frac{V_{ZrO_2} - (V_{ZrO_2+porous})}{V_{ZrO_2}} \tag{15}$$

Where $V_{ZrO_2+porous}$ is the volume of the ZrO_2 scaffold with porous, and V_{ZrO_2} is the total volume of the ZrO_2 bulk scaffold.

The ε_{eff} of porous dielectric structures is commonly estimated using volumetric mixing equations, similar to those applied in liquid mixtures. The permittivity behavior in solids is complex due to additional factors such as interfacial polarization (Maxwell-Wagner effect), charge trapping, and microstructural inhomogeneities [40]. The findings of Sihvola & Kong [40] demonstrated that, unlike liquids, where permittivity primarily depends on dipole interactions, in solids, factors like grain boundaries, void distributions, and localized field perturbations significantly influence the effective dielectric response. The validity of the volumetric mixing equation depends on pore shape, connectivity, and operating frequency. The simple linear model remains a reasonable approximation for low-frequency applications or materials with relatively uniform porosity, valid for isotropic, moderate-contrast systems like in this study, ZrO_2-air, where geometric and interaction effects are secondary. However, for highly porous or anisotropic materials, deviations from this model become significant, requiring the use of more comprehensive theoretical approaches. Equation (14) provides a first-order approximation based on volume fractions, assuming a homogeneous distribution of the porous phase. It's well-known that it doesn't depend only on the volume, but as an approximation, it can be justified. From the EM point of view, since in this study the porous scaffold dimensions are small compared to the wavelength (λ), the approximation in (14) can be used in this case. Specifically, it was verified that the pore dimensions are smaller than $\lambda/10$. While this simple mixing rule is often used, more advanced models, such as the Maxwell-Garnett and Bruggeman effective medium approximations, are frequently applied for dielectric mixtures, as they account for the shape and connectivity of inclusions within the solid [41]. The insights from Honrubia et al. [41] on liquid mixtures confirm that linear rules can approximate dielectric behavior when permittivity contrasts are modest, though nonlinear corrections (e.g., Gaussian volume fraction adjustments) may enhance accuracy at higher porosities. Given the agreement between the theoretical and simulated frequency predictions and expected trends, the chosen trend (14) to calculate the ε_{eff} strikes a balance between simplicity and physical plausibility while acknowledging potential refinements, such as shape-dependent depolarization or dispersion effects for future work.

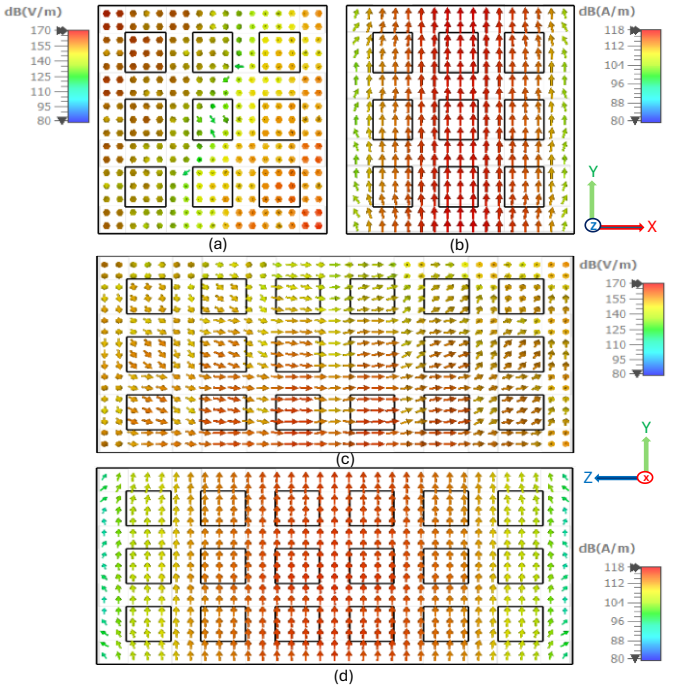

Fig. 4. Simulated electric (a, c) and magnetic (b, d) field distributions of the fundamental TM_{101} mode for the porous DR. Top views are shown in (a, b) and side views in (c, d).

Performing the same analysis as in the previous subsection (A. Modal Analysis of the Rectangular DR), a modal analysis of the porous DR was carried out. The resulting simulated field distributions are shown in Fig. 4. These distributions are similar to those of the fundamental mode of the bulk DR (Fig. 3). This

similarity is crucial, as it confirms that the fundamental mode remains stable and undistorted by the internal geometry. This preservation of the mode distribution validates the treatment of the porous scaffold as a homogeneous dielectric with an effective permittivity (ε_{eff}), where the pores primarily induce a frequency shift rather than a modal transformation. These results are in good agreement with theoretical predictions for rectangular resonators, confirming that the porous geometry modifies the operating frequency while preserving the EM field distributions of the DR.

The configuration was selected for this study, resulting in a porous size (W) of 3 × 3 mm and a spacing (D) of 2 mm. $V_{ZrO_2+porous}$ was found equal to 4204 mm^3, and V_{ZrO_2} equal to 9369 mm^3. The volume values were already calculated on Simplify software for the 3D printing designs. Therefore, using (15), the calculated value of φ was 0.551. That means 55.1% of the total volume is occupied by pores, indicating a relatively high level of porosity.

By calculating the φ, using the given permittivity values of ZrO_2 from Section III and vacuum ($\varepsilon_{vacuum} = 1$), the ε_{eff} of the porous scaffold was determined from (14) to be approximately 3.90. The reduction in ε_{eff} compared to ε_r, is attributed to the presence of air-filled pores, which leads to an increase in the resonant frequency, since it is inversely proportional to the square root of the effective permittivity ($f \propto 1/\sqrt{\varepsilon_{eff}}$). Therefore, the value of the frequency, substituting the ε_{eff} of the scaffold from (13) was 5.07 GHz.

In the simulations, the porous scaffold exhibited a higher resonant frequency than the bulk resonator. Specifically, the simulated resonant frequency of the porous structure was 5.54 GHz, compared to 3.66 GHz for the bulk resonator, whereas the theoretical value from (13) is 5.07 GHz. The observed discrepancy between theoretical and simulated results is mainly attributed to the limitations of the ε_{eff} approximation when applied to porous solid structures, as previously discussed. Nevertheless, this approach provides a first approximation, yields a consistent conclusion, and correctly predicts the expected increase in frequency with porosity.

This frequency shift is consistent with the theoretical expectation, as the ε_{eff} of the porous structure is lower than that of the bulk material. These results demonstrate that the porous scaffold can effectively act as a DR. Consequently, higher porosity results in a lower ε_{eff}, leading to higher resonant frequencies.

V. Sensing Principle

A. Influence of HA Layers in Resonant Frequencies of SenScaffolds

The macroscopic geometry of the scaffold plays a crucial role in regulating the kinetics of cell growth and, consequently, the formation of in vitro tissue [42]. Notably, bone cells tend to spontaneously grow from the interior to the exterior of the scaffold in a uniform manner in all directions, gradually filling the porous structure [43]. In this context, bone cell growth could alter the effective permittivity of the porous scaffold, resulting in detectable shifts in its resonant frequency. These shifts could then be used to monitor cellular regeneration.

In this work, ZrO_2 was used as the SenScaffold material, while the HA was chosen to simulate bone regeneration due to its chemical similarity to the mineral component of natural bone [32]. In this proof-of-concept study, the SenScaffold was modeled as a non-degradable structure, assuming that the PLA-ZrO_2 composite remains mechanically stable during the early bone-healing window (days to weeks). This is reasonable because PLA degrades very slowly in vivo, typically over months, much longer than the timescale of interest [44]. The bone growth model, therefore, varied only the HA content to isolate its effect on the EM response. Different models of the porous scaffold were simulated, with uniform HA layers added both to the exterior of the structure and inside the pores. Specifically, models with HA layers of 0.25 mm, 0.5 mm, 0.75 mm, 1 mm, and 1.25 mm were considered. The same porous scaffold design as in Fig. 2 is shown in Fig. 5 with HA layers (H) of 1 mm added in a cross-sectional view, resulting in $L_x = L_y = 19$ mm and $L_z = 34$ mm total outer dimensions. All the scaffold models with HA layers were simulated with the eigenmode CST Studio.

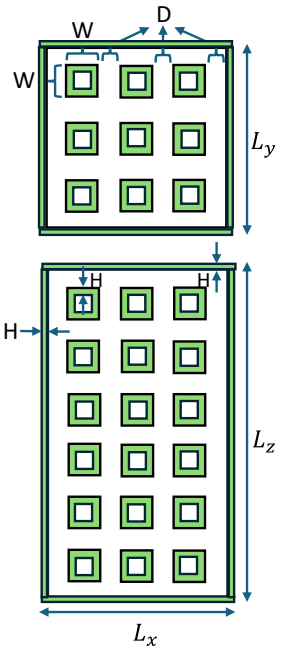

Fig. 5. Top (above) and side (below) cross-sectional views of the porous SenScaffold with simulated HA layers of thickness *H*.

The fundamental-mode resonant frequencies from eigenmode simulations are plotted in Fig. 6. Increasing the HA layer thickness, simulating bone growth, results in a gradual decrease in the resonant frequency. Specifically, the resonant frequency decreases from 5.02 GHz for a 0.25 mm HA layer to 3.76 GHz for a 1.5 mm HA layer, with intermediate values of 4.63 GHz, 4.29 GHz, 4.04 GHz, and 3.86 GHz corresponding to HA thicknesses of 0.5, 0.75, 1, and 1.25 mm, respectively.

According to the plot, initial findings suggest that the resonant frequency's dependence on the HA layers can be approximated by an inversely proportional function. This

behavior underscores the scaffolds' ability to exhibit measurable frequency changes, thereby enabling the detection and monitoring of the bone regeneration process. This reinforces the concept that scaffold-based DRs can serve as non-invasive biosensors for tracking events in the human body. However, the results reveal that the sensitivity of the system slightly decreases as the HA layer thickness increases, making frequency discrimination more challenging at larger HA depositions. Nevertheless, this limitation is not critical for the intended application, as the most relevant scenario is detecting the early stage of bone regeneration, which occurs on a short timescale of only a few days, being difficult to monitor with conventional imaging methods due to practical issues, such as the cost and inconvenience for the patient. This is precisely when the scaffold exhibits the strongest frequency shift response, allowing prompt detection of potential issues such as poor integration or scaffold detachment.

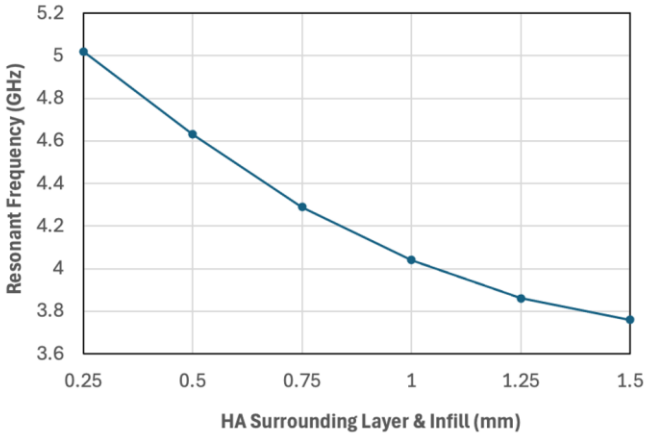

Fig. 6. Fundamental resonant frequency of the porous SenScaffold as a function of the HA layer thickness (H).

The same analysis as in Section IV (B. Porous Dielectric Resonator) was conducted, but now for the porous DR incorporated with HA. To find the ε_{eff}, now the equation becomes:

$$\varepsilon_{eff} = (1 - \varphi - V_{HA})\varepsilon_{r1} + \varphi\varepsilon_{vacuum} + V_{HA}\varepsilon_{r2} \quad (16)$$

The volume of HA is introduced and is given by:

$$V_{HA} = \frac{V_{total} - V_{ZrO_2+porous}}{V_{total}} \quad (17)$$

Where V_{total} is the volume of the composite porous structure (ZrO_2 + pores + HA (interior+exterior)), as shown in Fig. 5.

The φ now is given by:

$$\varphi = \frac{V_{ZrO_2} - (V_{total} - HA_{exterior})}{V_{ZrO_2}} = \frac{V_{vacuum}}{V_{ZrO_2}} \quad (18)$$

The $HA_{exterior}$ was calculated from:

$$HA_{exterior} = V_{ZrO_2+HA} - V_{ZrO_2} \quad (19)$$

Where V_{ZrO_2+HA} is the volume of the composite solid structure (ZrO_2 + HA) without the porous, to calculate the $HA_{exterior}$, which is the volume of HA deposited around the exterior of the structure.

V_{total} was given from the Simplify software, $V_{total} = 9822\ mm^3$. Using the (17) and the value of $V_{ZrO_2+porous}$ (4204 mm^3) from the previous section, $V_{HA} = 0.572$, and in terms of volume, multiplying this value by the total composite volume (9822 mm^3) = 5618 mm^3, meaning that HA constitutes 57.2% of the/ total composite volume (V_{total}). According to (19), the value of $V_{ZrO_2+HA} = 12274\ mm^3$, and the value of V_{ZrO_2} (9369 mm^3) from the previous section, the $HA_{exterior} = 2905\ mm^3$. Applying (18), the resulting φ was determined to be 0.262. This value was then used in (16) to calculate the ε_{eff}, considering ε_{r1}, the permittivity of the ZrO_2, and ε_{r2} the permittivity of HA, given from Section III, was found to be 4.05. Therefore, the value of the frequency, substituting the new ε_{eff} from (13) of the porous scaffold incorporated with HA is 4.5 GHz.

Since the HA occupy the 57.2% of the total composite volume, the remaining 42.8% corresponds to the porous ZrO_2 structure, which includes both the solid framework and the vacuum-filled pores. Therefore, the composite is comprised of three phases: ZrO_2 (solid), vacuum (pores), and HA. From (18), $V_{vacuum} = 2455\ mm^3$, which means vacuum-filled pores occupy 25%. Then since:

$$V_{ZrO_2-porous} = V_{ZrO_2+porous} - V_{vacuum} \quad (20)$$

Where $V_{ZrO_2-porous}$ is the ZrO_2 scaffold without the porous and was equal to $6914\ mm^3$, which means ZrO_2 constitutes 70.4% of the total volume. Nevertheless, because HA is added around and inside the structure, HA is both external and internal, while ZrO_2 scaffold and air pores is the structure before HA. Then the correct percentages within the final composite, only what is inside should be considered:

$$V_{ZrO_2-porous} = V_{total} - (V_{HA} + V_{vacuum}) \quad (21)$$

$V_{ZrO_2-porous}$ calculated from (21) = $1749\ mm^3$, which means 17.8% of the total volume. Based on the composite volume $V_{total} = 9822\ mm^3$, the final structure consists of approximately 57.2% HA, 25.0% vacuum (porosity), and 17.8% ZrO_2 by volume. These percentages reflect the contributions of each material phase within the composite scaffold after HA deposition, including both internal infiltration and external coating.

In the simulations, the porous scaffold with HA exhibited a resonant frequency of 4.04 GHz, which corresponds to a modest frequency shift of approximately 10% from the theoretical value of 4.5 GHz, indicating good agreement with the expected trend based on the theoretical model. The frequency shift is consistent with the theoretical expectation, as the frequency of the porous structure coated by HA (4.5 GHz) is lower than that of the porous ZrO_2 structure without the HA (5.07 GHz), since the porosity is lower.

B. Coaxial Probe/SenScaffold

Once the sensing capability of the isolated resonator has been demonstrated, the next step is to develop a proof-of-concept in which the resonator is interrogated wirelessly. To this end, in this work we focus on the design of a system based on a near-field probe coupled to the Senscaffold. In this first study, free space between the two elements is considered. Although this represents only an initial step, it is a necessary one, since it allows us to evaluate the coupling level between the two components of the system and to verify whether the detection trends predicted by theory and simulations are also observed experimentally. In practical applications, the proposed SenScaffold would be used for long-bone regeneration, where very thin layers of human tissues (skin, muscle, fat) would exist between the probe and the device. At this stage, such tissues have not been included in order to avoid additional sources of complexity that could hinder the proper verification of the detection fundamentals. In a more realistic scenario, distances could be similar, but it must be emphasized that this proof of concept has inherent limitations due to the absence of human tissue effects. Once the basic operation of the system is demonstrated in this article, more complete models including human tissues will be considered in future work, as discussed in Section VII.

The setup consists of a porous DR SenScaffold and a near-field coaxial probe for interrogation, as shown in Fig. 7, along with its relevant geometric parameters. The configuration was optimized using CST Studio Suite to ensure efficient magnetic coupling and mode excitation. H_{pin} and H_{Coax} denote the heights of the pin and the coaxial connector, respectively. PS_{gap} represents the gap between the pin and the scaffold. L_{GP} and W_{GP} correspond to the length and width of the ground plane, respectively, while D_{pin} and D_{coax} refer to the diameters of the inner pin and the outer conductor of the coaxial connector. The signal is altered based on the response of the SenScaffold. Furthermore, the design must account for possible variations in the relative orientation between the SenScaffold and the probe.

To effectively excite the DR's modes within the scaffold, the near-field coaxial probe was employed. In the context of DRs, efficient excitation of TM modes typically requires strong magnetic coupling between the external source and the resonator, as described previously in Section IV (A. Modal Analysis of the Rectangular Bulk DR). TM modes are characterized by a magnetic field component lying in the plane perpendicular to the electric field, and their excitation depends heavily on the alignment and continuity of the magnetic field at the interface between the source and the resonator. The coaxial probe was thus strategically chosen and positioned near the center of the porous scaffold to maximize coupling efficiency, where the electric field is maximum. Its geometry enables the generation of magnetic fields that can penetrate the scaffold and align with its internal resonant field structure, thereby supporting TM mode excitation via magnetic interaction. This theoretical framework underpins the subsequent simulation analysis, which verifies the expected field distribution and coupling behavior.

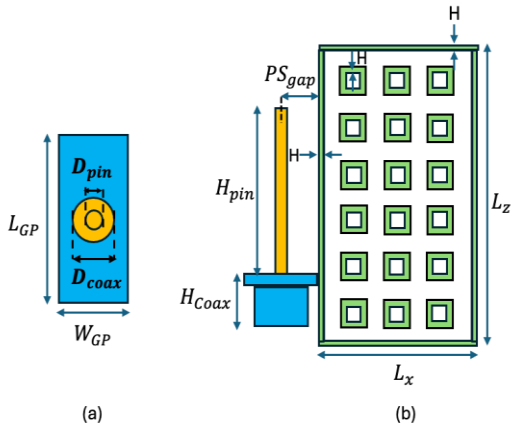

Fig. 7. Near-field interrogation setup: (a) top view of the coaxial probe and (b) side view of the probe-scaffold configuration. Geometrical parameters: $H_{pin} = 17\ mm$, $H_{Coax} = 7.8mm$, $PS_{gap} = 3.5\ mm$, $L_{GP} = 16\ mm$, $W_{GP} = 5.7\ mm$, $D_{pin} = 1.25\ mm$, and $D_{coax} = 4.1mm$. H is the thickness of the HA layers.

For this purpose, the coaxial probe was simulated in close proximity to the scaffold's center. The use of the coaxial probe inherently introduces proximity-dependent coupling effects that influence the absolute resonant response of the DR. When positioned close to the SenScaffold, the probe perturbs the EM distribution through strong near-field interactions, leading to slight shifts in the measured resonance compared to the isolated resonator case. In this work, the probe position, orientation, and separation distance are kept constant across all configurations to ensure that the observed frequency variations are primarily governed by changes in the ε_{eff} of the scaffold, rather than by variations in probe-resonator coupling. As a result, the sensing trends associated with progressive HA incorporation remain clearly distinguishable despite the presence of coupling-induced perturbations. The distance between the probe and the scaffold (PS_{gap}) was set to 3.5 mm to ensure sufficient magnetic coupling for TM_{101} mode excitation while maintaining a realistic separation consistent with future in vivo applications involving tissue layers. Parametric simulations, performed on both bulk and porous structures, verified that the system response is equivalent in both cases since the fundamental mode distribution is preserved. These studies confirmed that variations within a reasonable range (up to 1 cm) provide a robust response where the resonant peaks remain clearly distinguishable.

The magnetic field distributions of both the coaxial probe and the porous ZrO_2 DR with 1 mm HA layers are shown in Fig. 8 and correspond to a cross-sectional cut (perpendicular to the z-axis) of the SenScaffold and probe geometry. The larger square regions in the figure represent the scaffold's structural support pillars (forming a 4×4 matrix), while the smaller square regions correspond to the internal voids of the 3×3 pore arrangement described previously. The pores appear reduced in size due to the presence of the 1 mm HA layer on both internal and external surfaces. The observed alignment of the magnetic field vectors in the same plane indicates that the probe effectively excites the resonator and supports the TM modes. In particular, the coaxial probe generates a magnetic field that

extends outward, which is in the same plane as the scaffold's magnetic field. The clear evidence of magnetic field continuity between the probe and the scaffold confirms efficient magnetic coupling, which is a key mechanism for exciting TM modes in this structure. In particular, it is confirmed that the magnetic field inside the SenScaffold corresponds to the distribution of its fundamental mode, as discussed in Section IV.B.

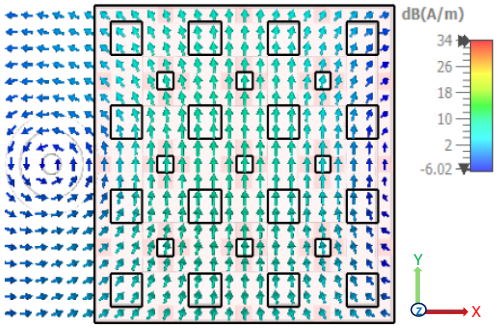

Fig. 8. Magnetic field distribution (cross-sectional view perpendicular to the *z* axis) demonstrating the electromagnetic coupling between the coaxial probe and the fundamental mode of the SenScaffold with a 1 mm HA layer.

It is evident that the porous ZrO_2 DR structure sustains the fundamental resonant mode according to Section IV (B. Porous Dielectric Resonator). The observed field patterns highlight the effective coupling between the probe and the scaffold, reinforcing the feasibility of the proposed system for self-sensing applications. Since HA has a relatively high dielectric constant, the overall permittivity of the scaffold increases, which in turn influences the confinement and propagation of EM fields within the resonator.

The use of a coaxial probe to excite the structure ensures efficient magnetic coupling, enabling real-time monitoring of resonance shifts. The introduction of the different HA layers, with their respective thicknesses, profoundly influences the resonant frequencies. The simulated frequency response of the setup under different scenarios is illustrated in Fig. 9: the isolated probe (blue curve), the inclusion of the bulk and porous ZrO_2 scaffold, and the scaffold with the simulated HA layers. All of them were simulated using the time-domain solver in CST Studio. The isolated probe demonstrates a resonant frequency that serves as a baseline for comparison. When integrated with the ZrO_2 scaffold, an additional resonant response emerges due to the interaction between the probe and the dielectric structure. In these cases, two distinct peaks are typically observed: the first corresponds to the resonance of the SenScaffold itself, while the second arises from the intrinsic resonance of the probe. The bulk ZrO_2 scaffold (black curve) serves as a clear reference for the coupled system, where the two distinct peaks are observed and the first peak has the lowest frequency of all the simulations which is consistent with its higher permittivity, as studied in Section IV. In the case of the porous scaffold without HA (yellow solid curve), both modes are also present; however, due to the strong coupling and the proximity of their resonant frequencies, the two peaks overlap, resulting in a single resonance with an increased bandwidth. Moreover, introducing HA layers of 1 mm (red dashed curve) and 1.5 mm (green dashed curve) reveals a trend where increased HA thickness correlates with lower resonant frequencies, highlighting the high sensitivity of the system.

It is worth noting that the observed frequency trend in the simulated results is consistent with the theory presented in Section IV (B. Porous Dielectric Resonator) and with the simulation results in Section V.A (Fig. 6), where the scaffold was examined independently, as an uncoupled resonator. The results have shown that the introduction of HA layers leads to a downward shift in the resonant frequencies from 4.2 GHz (HA 1 mm) to 3.95 GHz (HA 1.5 mm). However, a key distinction lies in the excitation conditions of the scaffold. In the theoretical analysis, the scaffold was considered in an uncoupled state, without any external excitation from a probe, thereby allowing for a clear and direct observation of the frequency shift solely due to changes in the scaffold's dielectric properties. In contrast, the simulations involve the integration of the scaffold using a coaxial probe, introducing coupling effects between the probe and the scaffold. Despite this coupling, which slightly modifies the absolute values of the resonant frequencies in the first resonance, the same downward trend with increasing HA thickness is observed. This consistency confirms that the underlying physical behavior remains valid even when probe-SenScaffold interactions are present. Therefore, the simulated results not only support the theoretical findings but also demonstrate the robustness of the frequency shift trend under practical excitation conditions.

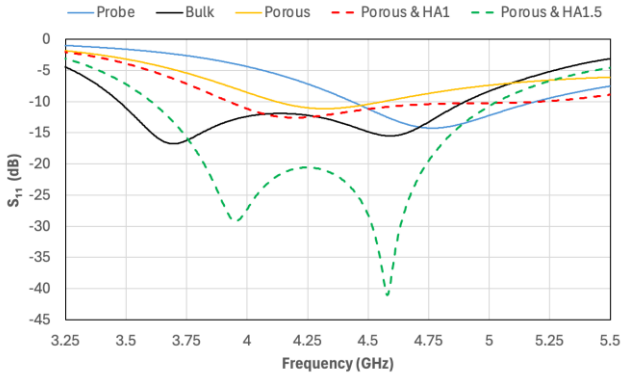

Fig. 9. Simulated Frequency response - Reflection coefficient ($|S_{11}|$) for the unloaded probe (blue), bulk ZrO_2 scaffold (black), porous ZrO_2 scaffold (yellow solid), and porous SenScaffold with HA layers of 1 mm (red dashed) and 1.5 mm (green dashed).

It is worth noting that the simulations of the probe-resonator system were carried out for different thicknesses of the layers that emulate bone regeneration. From a theoretical point of view, according to Section V.A, the device is expected to be more sensitive to thin layers (H < 1 mm), which are also the most relevant for the intended application, i.e., monitoring the early stages of regeneration (within days to weeks). However, due to the limitations and tolerances of the fabrication process—based on AM using PLA pellets loaded with HA—it was not feasible to print layers thinner than 1 mm. For this reason, the experimental proof of concept was performed with thicker layers, with the aim of verifying that the expected detection trends are still maintained under these conditions. Nevertheless, the proposed proof of concept addresses the monitoring of bone

regeneration by considering three distinct states: the bulk scaffold and two different stages of the regeneration process.

Overall, the simulated results demonstrate that scaffold geometry and material properties, including the HA layer thickness, profoundly influence the frequency response.

VI. Experimental Results

A. Prototypes

Following the design and simulation phases, the bulk ZrO_2, porous ZrO_2 scaffold, and porous ZrO_2 scaffolds incorporated with HA were fabricated using FDM 3D printing. The HA layers, incorporated both on the exterior of the scaffold and within the manufactured pores for this study, were designed with thicknesses of 1 mm and 1.5 mm. These layer thicknesses were selected considering the fabrication process limitations, as previously discussed in the simulation stage. All 3D-printed scaffold prototypes are shown in Fig. 10.

To assess the dimensional fidelity of the 3D-printed structures, the printed prototypes were measured and compared against the simulated dimensions. Specifically, for the bulk ZrO_2 and porous ZrO_2 scaffolds, the target layer height of 0.2 mm was successfully achieved, indicating excellent printability and process reliability.

For all scaffold types, pore size was measured using an opto-digital microscope (Olympus) by taking five measurements at different locations (top, bottom, and four sides) and calculating the overall average. The porous ZrO_2 scaffold exhibited a minor deviation, with a 5% error from the expected pore size, reflecting relatively high geometric accuracy. In contrast, the scaffolds with HA infill showed a greater deviation from the target pore sizes. For the 1 mm, the measured pores were smaller than intended (0.84 mm versus the target value of 1 mm). In the case of the 1.5 mm infill, the pores were nearly closed, as expected by design.

In addition to pore size, the height (*z*-axis) of the scaffolds was also evaluated, as it plays a crucial role in determining the effective dielectric properties of the structure. Across all scaffold types, the printed height closely matched the designed value, with an average deviation of only 1.5%. This minimal error is particularly important, as the height directly influences the overall permittivity of the scaffold, which in turn affects the EM field distribution and the resulting frequency response. The high accuracy in the vertical dimension thus contributes to the reliability of the simulated and experimental correlation.

These dimensional discrepancies, particularly in the HA-infused scaffolds, are attributed to the resolution limitations inherent in the FDM process, especially when printing complex and fine internal features. Such deviations help explain the observed shifts in the resonant frequencies of the different HA-infilled scaffolds, as the effective dielectric distribution and EM response are directly affected by pore geometry. Importantly, the fabrication process achieved its primary objective: the successful production of multiple scaffold variants with controlled differences in HA infill and outfill configurations.

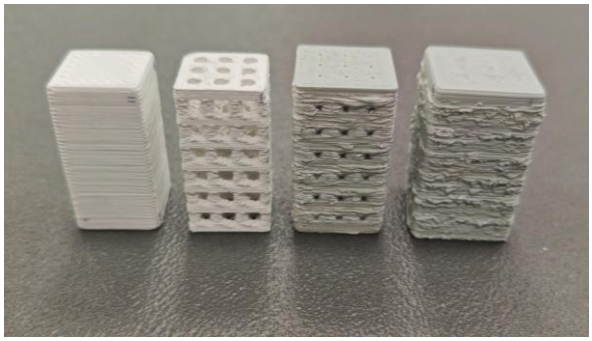

Fig. 10. 3D-printed scaffold prototypes (from left to right): bulk, porous SenScaffold ,and SenScaffolds with 1 mm and 1.5 mm HA layers.

B. Sensing Measurements

An experimental setup was designed to replicate the simulation conditions as closely as possible. For this purpose, a small PLA platform was fabricated using AM, on which each DR was placed and where the coaxial probe was fixed (Fig. 11). In this way, the same distance between the two elements of the system as in the simulations was maintained. The coaxial probe was implemented using a commercial SMA connector [45], which was connected to a VNA (Anritsu MS46122B) calibrated over the frequency range of 3.25 – 5.5 GHz to measure the probe's reflection coefficient $|S_{11}|$, coupled to the different DRs. The height of the coaxial probe pin was adjusted to match the design, and the PTFE surrounding the pin was kept to provide mechanical consistency.

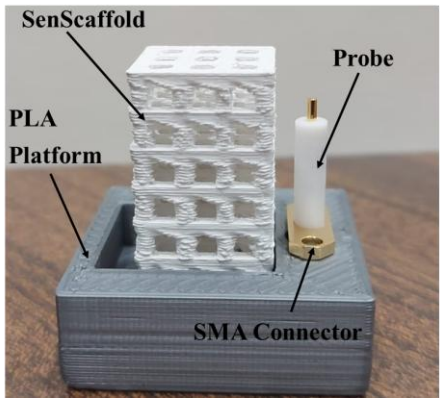

(a)

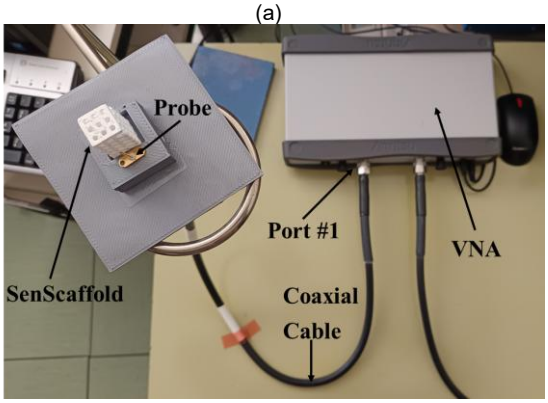

(b)

Fig. 11. Photographs of the experimental setup for the sensing measurements: (a) coaxial probe and SenScaffold positioned on the 3D-printed PLA platform, and (b) connection to the VNA via a coaxial cable.

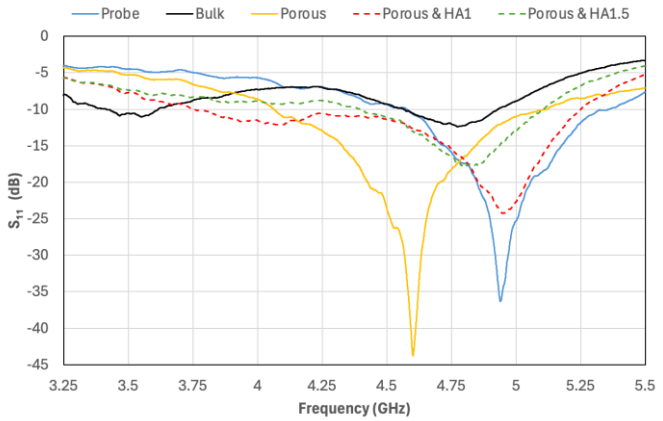

Fig. 12. Measured frequency response - Reflection coefficient ($|S_{11}|$) between unloaded probe (blue), bulk ZrO_2 scaffold/probe (black), porous ZrO_2 scaffold/probe (yellow) in solid line, porous ZrO_2 scaffold/probe + HA 1 mm layer (red), and ZrO_2 scaffold/probe + HA 1.5 mm layer (green) in dashed line.

The $|S_{11}|$ measurements presented in Fig. 12 demonstrate the reflection characteristics of various scaffold configurations. The coaxial probe (blue) itself exhibits a well-defined resonant response at 4.90 GHz, and its baseline response serves as a reference for evaluating changes introduced by the scaffold.

The introduction of the bulk and porous ZrO_2 scaffold significantly alters the probe's response, leading to a shift in resonant frequency. This confirms the interaction between the scaffold and the EM field generated by the probe. Both simulated (Fig. 9) and experimental results indicate a lower resonant frequency than with the probe alone, as expected due to the higher effective permittivity of ZrO_2. Each configuration exhibits two distinct resonant frequencies: the first corresponds to the scaffold mode, while the second reflects the pin mode, the same as Fig. 9. Notably, the porous ZrO_2 scaffold without HA inclusion (yellow curve) stands out at a resonance of 4.60 GHz and exhibits a pronounced resonance dip between the two dominant modes, indicative of a strong coupling effect between the pin and scaffold modes, resulting in enhanced impedance matching and sharper resonance. As HA is incrementally introduced into the porous ZrO_2 scaffolds, starting from 1 mm (red curve) to 1.5 mm (green), a consistent small frequency shift is observed. Table II presents the two resonance peaks for each configuration, enabling a more quantitative comparison. Specifically, the first peak shifts from 4.60 GHz (porous ZrO_2) to 4.10 GHz (HA 1 mm), and finally to 3.91 GHz (HA 1.5 mm). To determine the minimum frequency of each peak, the average of two frequency points was calculated, one on each side of the frequency corresponding to the minimum $|S_{11}|$ value. The experimental results confirm the trend observed in theory and simulations: (Section V: Sensing Principle) the presence of HA lowers the resonant frequency, supporting the hypothesis that increasing HA deposition alters the scaffold's effective permittivity by increasing HA content. The observed frequency shift follows an inversely proportional trend, as previously identified in theory, reinforcing the feasibility of using the scaffold as a self-sensing system for bone regeneration monitoring. Similarly, the second peak, where observed, also experiences a downward shift (e.g., from 4.95 GHz to 4.81 GHz), although with a less pronounced trend, but that's due to high coupling with the probe mode, and this could also be used for the detection of the different layers. Nevertheless, even small increments in HA layers noticeably affect the overall system response. In summary, it is important to highlight the significant differences observed between the SenScaffold without HA (porous ZrO_2) and the two prototypes that emulate different stages of regeneration (porous ZrO_2 with 1 mm and 1.5 mm HA layers).

TABLE II
RESONANT FREQUENCIES OF THE PROBE/SCAFFOLDS SETUP

Probe/Scaffolds	Minimum Frequency (GHz) Scaffold mode	Minimum Frequency (GHz) Probe mode
Probe	–	4.90
Porous ZrO_2	4.60 (coupled)	
Porous & HA 1	4.10	4.95
Porous & HA 1.5	3.91	4.81
Bulk ZrO_2	3.55	4.77

To facilitate a direct visual comparison between simulations and measurements, Fig. 13 presents the resonant frequencies extracted for the different SenScaffold configurations under the considered operating conditions. The figure illustrates a consistent downward shift in resonant frequency as HA layers are progressively introduced into the porous ZrO_2 scaffold and, most importantly, demonstrates close agreement between the simulated and measured resonant frequencies across all configurations. The maximum deviation between simulation and experiment remains below approximately 7% across all cases. This discrepancy is primarily attributed to the inherent tolerances of the FDM AM process, such as the 5% error in pore size and 1.5% deviation in structural height observed during the characterization of the prototypes. These results confirm the validity of the proposed sensing approach and the robustness of the EM models despite the minor geometric variations introduced during 3D printing.

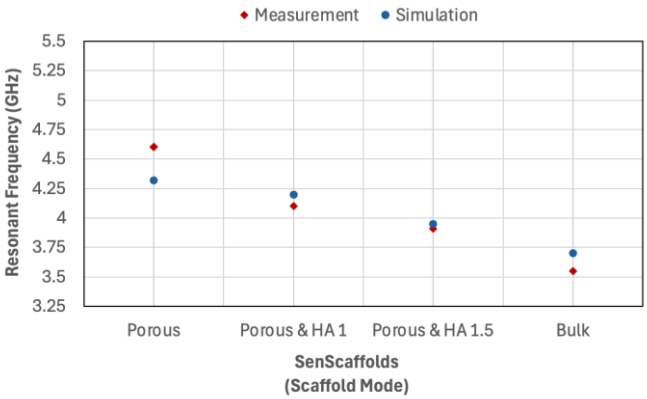

Fig. 13. Comparison of the measured and the simulated resonant frequencies for different SenScaffold configurations in the scaffold mode.

From the experimental results of the fundamental resonance frequency summarized in Table II, a sensitivity of 500 MHz/mm is obtained for HA growth up to 1 mm, and 380 MHz/mm for the interval between 1 and 1.5 mm. According to the measurements, the device sensitivity is clearly non-linear, exhibiting a higher detection capability during the initial stage of HA growth. This behavior is fully consistent with the analysis of the isolated resonator presented in Section V.A, where a stronger response to thin dielectric layers was predicted.

Regarding the experimental methodology, the use of a VNA enables precise and real-time monitoring of resonance frequency variations. In addition, repeatability was verified by performing systematic measurements on each face of the fabricated prototypes, with no significant variations observed in the EM response.

Additionally, as discussed in Section III (3D Printing and Dielectric Characterization), the HA material exhibits significantly higher dielectric losses than ZrO_2. This increased loss tangibly affects the resonance behavior, as observed by the progressive flattening of the $|S_{11}|$ curves with higher HA content. Thus, the measured trends in both frequency shift and peak broadening are jointly explained by the combined influence of increased permittivity and material losses introduced by HA.

Finally, it is important to note that this work has mainly focused on detection based on a primary parameter, namely the fundamental resonant frequency of the SenScaffold. However, the above experimental considerations also open the possibility of exploiting secondary features of the reflection coefficient of the complete system, such as the amplitude of the first resonance or the frequency of the second peak, to achieve improved detection and discrimination of the regenerated layer thickness. In a subsequent step, even Machine Learning (ML) techniques could be employed, since their ability to enhance the sensitivity of passive EM sensor responses has been recently demonstrated [46].

VII. Comparison of the Detection Techniques

As previously discussed, this work focuses on the most fundamental MW resonator sensing technique, which is the tracking of the resonant frequency variation. However, the same SenScaffold structure allows for more complex interrogation schemes that could provide enhanced performance, such as detecting the frequency shift of the second peak or monitoring amplitude variations. Recently, alternative interrogation methods based on magnitude or phase detection at a single frequency have been developed [47]−[48]. These single-frequency techniques generally offer higher sensitivities by exploiting the high slope of the resonance response near poles and zeros. As a complementary approach, ML models have demonstrated substantial improvements in sensitivity, even when using basic frequency-variation detection and low-cost electronic readers [46].

Regarding system complexity and cost, it is essential to distinguish between two current trends: the use of laboratory instrumentation, primarily VNAs, and the development of interrogation systems based on consumer electronics, typically utilizing voltage-controlled oscillators (VCOs) and power detectors [46]−[48]. VNA-based detection is primarily suited for initial experimental validation in a laboratory environment [20]. Due to its high cost and bulky size, it is not practical for the development of commercial clinical devices. In contrast, electronics based on off-the-shelf components offer significant advantages in terms of simplicity and affordability [46]−[48]. While this study employs a VNA because the technology is in an early proof-of-concept stage, the perspective is to develop dedicated low-cost electronic readers in future phases.

In this context, it is important to highlight that phase and magnitude-variation techniques require only a fixed frequency from the oscillator [47]−[48]. Conversely, the frequency-variation technique utilized in this work necessitates a frequency sweep performed by a VCO [46]. Another critical trade-off regarding complexity and portability concerns the choice between reflection (monostatic) or transmission (bistatic) measurement configurations. Reflective-mode configurations allow for single-antenna or single-port setups, which are inherently more portable [46]−[47]. However, the primary challenge of monostatic systems is the requirement for additional hardware, such as circulators or couplers, to separate the incident and reflected signals, which can increase the cost and complexity of the electronics. On the other hand, transmission-based schemes utilize bistatic arrangements that eliminate the need for a circulator but result in a larger physical footprint and reduced portability due to the dual-antenna requirement [48].

In summary, this work utilized frequency-tracking via laboratory instrumentation for robust validation. However, to advance the system toward clinical application, future iterations will explore combining frequency-tracking with amplitude detection and ML techniques to enhance sensitivity while utilizing affordable consumer electronics. Despite the added complexity of a circulator, a monostatic system based on a single near-field probe remains the preferred choice for this specific application. A single probe can be easily fixed to the patient's skin, ensuring it remains stationary during movement and providing a far more portable and practical solution for continuous monitoring.

VIII. Future Work & Perspectives

While the results presented in this work demonstrate the feasibility of porous DRs as self-sensing scaffolds, several aspects must be addressed before the SenScaffold concept can be translated into practical biomedical applications. In particular, the presence of biological tissues such as skin, muscle, fat, and body fluids between the external interrogating device and the SenScaffold may attenuate or distort the EM response, potentially affecting sensitivity and measurement accuracy. In addition, potential scaffold hydration and fluid infiltration within the porous network may introduce baseline shifts in the resonant response and will be evaluated in future studies.

This work has laid the foundations for the simultaneous use of DRs as both scaffolds and passive MW sensors. The

technology shows promising potential. Although the results obtained so far are encouraging, the proof-of-concept demonstrations have been conducted in controlled environments.

Future research will therefore focus on validating the proposed approach under more realistic conditions, closer to clinical practice. In particular, four main directions are envisaged: first, exploring an alternative to the HA-pellet-based AM process, in order to fabricate thinner layers of bone regeneration and thus determine the sensitivity limits; second, developing a more realistic experimental setup that includes human tissues between the probe and the Senscaffold. Specifically, long bones will be considered, taking into account the average dielectric properties and dimensions of the different tissue layers and body fluids, with full-wave simulations performed prior to experimental implementation to ensure proper signal detection in such environments; third, applying ML techniques to accurately estimate the evolution of bone regeneration, even in complex and realistic scenarios and finally, transitioning from laboratory VNAs to portable, low-cost electronic readers based on consumer electronics to facilitate real-time monitoring in clinical settings. These developments will move the proposed SenScaffold concept closer to a clinically relevant, non-invasive monitoring platform for bone regeneration.

IX. Conclusions

This study successfully demonstrates the proof of concept for a 3D-printed porous DR that functions as a self-sensing scaffold, named SenScaffold, for bone regeneration. The SenScaffold is capable of detecting changes in its surrounding environment by measuring shifts in resonant frequencies.

To achieve this proof of concept, a modal analysis was first conducted on both the bulk and porous DRs. It was concluded that both possess similar mode distributions. In particular, the fundamental mode in both cases is TM_{101}, exhibiting similar EM field distributions. Theoretical equations for the modal analysis were developed and validated through full-wave simulations. As expected, the primary effect of introducing pores into the structure is a decrease in the resonance frequencies. This effect was also theoretically modeled by calculating the "effective" permittivity and verified through simulation.

The next step involved demonstrating that the porous DR is sensitive to environmental variations while maintaining its scaffold structure. Considering its application in bone regeneration, different uniform layers of HA, the main component of bone with ε_r similar to bone tissue, were applied. Theoretical analysis was conducted to study the variation of the effective permittivity of the structure with the inclusion of HA layers. A decrease in the fundamental frequency was observed as the thickness of the HA layers increased. Modal simulations confirmed these results, showing that the fundamental mode's resonance frequency decreases with increasing HA layer thickness.

Finally, to complete the proof of concept, an interrogation system was designed based on a coaxial proximity probe. This design enables the non-contact measurement of the SenScaffolds' response, serving as a preliminary approach to what would be implemented in a real system. Using the FDM AM technique, both the bulk DR and the SenScaffold were printed in ZrO_2-reinforced PLA. Additionally, to simulate different stages of bone regeneration, three SenScaffolds were printed with overlapping layers of HA-reinforced PLA.

All fabricated prototypes were measured using the experimental setup based on the coaxial probe connected to the VNA, which enables precise and real-time monitoring of these resonance frequency variations. Reflection coefficient measurements confirm that the SenScaffolds interact strongly with the near-field coaxial probe, leading to distinct two resonances. The first resonant peak corresponds to the fundamental mode of the DRs. The introduction of HA layers into the porous scaffolds resulted in a progressive downshift of the lower-frequency resonance from 4.60 GHz (bulk resonator) to 4.10 and 3.91 GHz for HA thicknesses of 1 mm and 1.5 mm, respectively, demonstrating a sensitivity to HA-induced permittivity changes. From these results, a sensitivity of 500 MHz/mm is obtained for HA growth up to 1 mm and 380 MHz/mm for the interval between 1 and 1.5 mm, demonstrating a non-linear behavior that is more sensitive during the initial stages. This trend, consistent with simulation results, confirms the scaffold's capability to detect subtle variations in HA content, validating its function as a non-invasive sensor for HA layers.

Overall, the theoretical and experimental studies in this paper demonstrate that a porous DR can be effectively adapted as a bone scaffold with integrated sensing capabilities, named SenScaffold. The ability to monitor bone regeneration via EM interrogation represents a significant advancement, offering a non-invasive and scalable approach for real-time biomedical diagnostics. This work should be understood as a first, necessary step toward a more realistic in vivo monitoring system, and its main contribution is to prove that a porous DR can function as a scaffold and respond to controlled changes in a bone-like material. Future research will focus on validating the system under realistic biological environments and exploring portable, low-cost interrogation electronics to move the SenScaffold concept closer to clinical practice.

References

[1] A. Marrella *et al.*, "Engineering vascularized and innervated bone biomaterials for improved skeletal tissue regeneration," *Mater. Today*, vol. 21, no. 4, pp. 362–376, May 2018, doi: 10.1016/j.mattod.2017.10.005

[2] S. S. Lee, X. Du, I. Kim, and S. J. Ferguson, "Scaffolds for bone-tissue engineering," *Matter*, vol. 5, no. 9, pp. 2722–2759, Sep. 2022, doi: 10.1016/j.matt.2022.06.003

[3] N. Abbasi, S. Hamlet, R. M. Love, and N.-T. Nguyen, "Porous scaffolds for bone regeneration," *J. Sci. Adv. Mater. Devices*, vol. 5, no. 1, pp. 1–9, Mar. 2020, doi: 10.1016/j.jsamd.2020.01.007

[4] M. Mabrouk, H. H. Beherei, and D. B. Das, "Recent progress in the fabrication techniques of 3D scaffolds for tissue engineering," *Mater. Sci. Eng. C*, vol. 110, p. 110716, May 2020, doi: 10.1016/j.msec.2020.110716

[5] I. M. Adel, M. F. ElMeligy, and N. A. Elkasabgy, "Conventional and Recent Trends of Scaffolds Fabrication: A Superior Mode for Tissue Engineering," *Pharmaceutics*, vol. 14, no. 2, p. 306, Jan. 2022, doi: 10.3390/pharmaceutics14020306

[6] A. Farazin, C. Zhang, A. Gheisizadeh, and A. Shahbazi, "3D bio-printing for use as bone replacement tissues: A review of biomedical application,"

Biomed. Eng. Adv., vol. 5, p. 100075, Jun. 2023, doi: 10.1016/j.bea.2023.100075

[7] X. Su, T. Wang, and S. Guo, "Applications of 3D printed bone tissue engineering scaffolds in the stem cell field," *Regen. Ther.*, vol. 16, pp. 63–72, Mar. 2021, doi: 10.1016/j.reth.2021.01.007

[8] X. Yuan *et al.*, "Recent Advances in 3D Printing of Smart Scaffolds for Bone Tissue Engineering and Regeneration," *Adv. Mater.*, vol. 36, no. 34, p. 2403641, Aug. 2024, doi: 10.1002/adma.202403641

[9] C. Wang *et al.*, "3D printing of bone tissue engineering scaffolds," *Bioact. Mater.*, vol. 5, no. 1, pp. 82–91, Mar. 2020, doi: 10.1016/j.bioactmat.2020.01.004

[10] K. Prem Ananth and N. D. Jayram, "A comprehensive review of 3D printing techniques for biomaterial-based scaffold fabrication in bone tissue engineering," *Ann. 3D Print. Med.*, vol. 13, p. 100141, Feb. 2024, doi: 10.1016/j.stlm.2023.100141

[11] Z. Qu, J. Yue, N. Song, and S. Li, "Innovations in three-dimensional-printed individualized bone prosthesis materials: revolutionizing orthopedic surgery: a review," *Int. J. Surg.*, vol. 110, no. 10, pp. 6748–6762, Oct. 2024, doi: 10.1097/JS9.0000000000001842

[12] S. Raisian, H. R. Fallahi, K. S. Khiabani, M. Heidarizadeh, and S. Azdoo, "Customized Titanium Mesh Based on the 3D Printed Model vs. Manual Intraoperative Bending of Titanium Mesh for Reconstructing of Orbital Bone Fracture: A Randomized Clinical Trial," *Rev. Recent Clin. Trials*, vol. 12, no. 3, Nov. 2017, doi: 10.2174/1574887112666170821165206

[13] D. M. Simoneti, T. Pereira-Cenci, and M. B. F. Dos Santos, "Comparison of material properties and biofilm formation in interim single crowns obtained by 3D printing and conventional methods," *J. Prosthet. Dent.*, vol. 127, no. 1, pp. 168–172, Jan. 2022, doi: 10.1016/j.prosdent.2020.06.026

[14] R. Winarso, P. W. Anggoro, R. Ismail, J. Jamari, and A. P. Bayuseno, "Application of fused deposition modeling (FDM) on bone scaffold manufacturing process: A review," *Heliyon*, vol. 8, no. 11, p. e11701, Nov. 2022, doi: 10.1016/j.heliyon.2022.e11701

[15] L. Zhou *et al.*, "Additive Manufacturing: A Comprehensive Review," *Sensors*, vol. 24, no. 9, p. 2668, Apr. 2024, doi: 10.3390/s24092668

[16] Y. Yang *et al.*, "X-ray imaging optimization of 3D tissue engineering scaffolds via combinatorial fabrication methods," *Biomaterials*, vol. 29, no. 12, pp. 1901–1911, Apr. 2008, doi: 10.1016/j.biomaterials.2007.12.042

[17] Istituto Nazionale per la Ricerca sul Cancro, Largo R. Benzi, 10, 16132 Genova, Italy *et al.*, "Biodegradation of porous calcium phosphate scaffolds in an ectopic bone formation model studied by X-ray computed microtomograph," *Eur. Cell. Mater.*, vol. 19, pp. 136–146, Mar. 2010, doi: 10.22203/eCM.v019a14

[18] H. Hallil *et al.*, "Passive Resonant Sensors: Trends and Future Prospects," *IEEE Sens. J.*, vol. 21, no. 11, pp. 12618–12632, Jun. 2021, doi: 10.1109/JSEN.2021.3065734

[19] F. Alruwaili, K. Cluff, J. Griffith, and H. Farhoud, "Passive Self Resonant Skin Patch Sensor to Monitor Cardiac Intraventricular Stroke Volume Using Electromagnetic Properties of Blood," *IEEE J. Transl. Eng. Health Med.*, vol. 6, pp. 1–9, 2018, doi: 10.1109/JTEHM.2018.2870589

[20] M. G. Mayani, F. J. Herraiz-Martinez, J. M. Domingo, and R. Giannetti, "Resonator-Based Microwave Metamaterial Sensors for Instrumentation: Survey, Classification, and Performance Comparison," *IEEE Trans. Instrum. Meas.*, vol. 70, pp. 1–14, 2021, doi: 10.1109/TIM.2020.3040484

[21] "Guidelines for Limiting Exposure to Electromagnetic Fields (100 kHz to 300 GHz)," *Health Phys.*, vol. 118, no. 5, pp. 483–524, May 2020, doi: 10.1097/HP.0000000000001210

[22] R. A. Alahnomi *et al.*, "Review of Recent Microwave Planar Resonator-Based Sensors: Techniques of Complex Permittivity Extraction, Applications, Open Challenges and Future Research Directions," *Sensors*, vol. 21, no. 7, p. 2267, Mar. 2021, doi: 10.3390/s21072267

[23] A. Ojha, A. Yousaf, and L. M. Reindl, "Characterization of dielectric resonator as a passive mechanical sensing element," *in* Proc. 2012 6th Int. Conf. Sensing Technol. (ICST), Kolkata: IEEE, Dec. 2012, pp. 219–225, doi: 10.1109/ICSensT.2012.6461674

[24] A. E. Omer *et al.*, "Multiple-Cell Microfluidic Dielectric Resonator for Liquid Sensing Applications," *IEEE Sens. J.*, vol. 21, no. 5, pp. 6094–6104, Mar. 2021, doi: 10.1109/JSEN.2020.3041700

[25] M. Tlili, F. Deshours, G. Alquié, H. Kokabi, S. Hardinata, and F. Koskas, "Microwave Resonant Sensor for Non-invasive Characterization of Biological Tissues," *IRBM*, vol. 39, no. 6, pp. 445–450, Dec. 2018, doi: 10.1016/j.irbm.2018.10.013

[26] L. Robins *et al.*, "3D-Printed Dielectric Resonators for Quasi-TE112 Mode Singlets, Doublets and Dual-Mode Filters," *IEEE Access*, vol. 10, pp. 130326–130338, 2022, doi: 10.1109/ACCESS.2022.3228764

[27] R. Shamsaee Malfajani, R. Damansabz, S. Bodkhe, D. Therriault, J.-J. Laurin, and M. S. Sharawi, "3-D-Printed Encapsulated Dielectric Resonator Antennas with Large Operation Frequency Ratio for Future Wireless Communications," *IEEE Open J. Antennas Propag.*, vol. 5, no. 5, pp. 1351–1364, Oct. 2024, doi: 10.1109/OJAP.2024.3416399

[28] G. M. Rocco, P. Barmuta, X. Bao, D. Schreurs, and M. Bozzi, "Efficient approach for dielectric permittivity measurements of liquids adopting a 3D-printed cavity resonator," *Microw. Opt. Technol. Lett.*, vol. 63, no. 11, pp. 2797–2802, Nov. 2021, doi: 10.1002/mop.32979

[29] M. G. Mayani, F. J. Herraiz-Martinez, J. M. Domingo, R. Giannetti, and C. R.-M. Garcia, "A Novel Dielectric Resonator-Based Passive Sensor for Drop-Volume Binary Mixtures Classification," *IEEE Sens. J.*, vol. 21, no. 18, pp. 20156–20164, Sep. 2021, doi: 10.1109/JSEN.2021.3094904

[30] A. H. Kalhori, T. Kim, and W. S. Kim, "Enhanced RF response of 3D-printed wireless LC sensors using dielectrics with high permittivity," *Flex. Print. Electron.*, vol. 8, no. 1, p. 015013, Mar. 2023, doi: 10.1088/2058-8585/acb722

[31] P. Sofokleous, E. Paz, and F. J. Herraiz-Martínez, "Design and Manufacturing of Dielectric Resonators via 3D Printing of Composite Polymer/Ceramic Filaments," *Polymers*, vol. 16, no. 18, p. 2589, Sep. 2024, doi: 10.3390/polym16182589

[32] P. O. Etinosa *et al.*, "In-depth review of synthesis of hydroxyapatite biomaterials from natural resources and chemical regents for biomedical applications," *Arab. J. Chem.*, vol. 17, no. 12, p. 106010, Dec. 2024, doi: 10.1016/j.arabjc.2024.106010

[33] V. R. Sivaperumal, R. Mani, V. Polisetti, K. Aruchamy, and T. Oh, "Synthesis of Hydroxyapatite (HAp)-Zirconia Nanocomposite Powder and Evaluation of Its Biocompatibility: An In Vitro Study," *Appl. Sci.*, vol. 12, no. 21, p. 11056, Nov. 2022, doi: 10.3390/app122111056

[34] "QWED - Split-Post Dielectric Resonator". Accessed: Jan. 10, 2026. [Online]. Available: https://qwed.eu/measurement-setups/split-post-dielectric-resonators-spdr/

[35] "Compact USB Vector Network Analyzer | Anritsu America". Accessed: Jan. 10, 2026. [Online]. Available: https://www.anritsu.com/en-us/test-measurement/products/ms46122b

[36] R. S. Yaduvanshi and H. Parthasarathy, *Rectangular Dielectric Resonator Antennas: Theory and Design*. New Delhi: Springer India, 2016. , doi: 10.1007/978-81-322-2500-3

[37] D. K. Cheng, *Field and wave electromagnetics*, Second edition. in World student series edition. Edinburgh: Pearson, 2014.

[38] R. Kumar Mongia and A. Ittipiboon, "Theoretical and experimental investigations on rectangular dielectric resonator antennas," *I*EEE Trans. Antennas Propag., vol. 45, no. 9, pp. 1348-1356, Sept. 1997, doi: 10.1109/8.623123

[39] "CST Studio Suite 3D EM simulation and analysis software". Accessed: Jan. 10, 2026. [Online]. Available: https://www.3ds.com/products-services/simulia/products/cst-studio-suite/

[40] A. H. Sihvola and J. A. Kong, "Effective permittivity of dielectric mixtures," *IEEE Trans. Geosci. Remote Sens.*, vol. 26, no. 4, pp. 420–429, Jul. 1988, doi: 10.1109/36.3045

[41] M. Monteagudo Honrubia, F. J. Herraiz-Martínez, and J. Matanza Domingo, "A Machine Learning approach for enhancing permittivity mixing rules of binary liquids with a Gaussian modification and a new interaction factor estimation," *J. Mol. Liq.*, vol. 399, p. 124290, Apr. 2024, doi: 10.1016/j.molliq.2024.124290

[42] F. Mukasheva, L. Adilova, A. Dyussenbinov, B. Yernaimanova, M. Abilev, and D. Akilbekova, "Optimizing scaffold pore size for tissue engineering: insights across various tissue types," *Front. Bioeng. Biotechnol.*, vol. 12, p. 1444986, Nov. 2024, doi: 10.3389/fbioe.2024.1444986

[43] Y. Guyot, I. Papantoniou, Y. C. Chai, S. Van Bael, J. Schrooten, and L. Geris, "A computational model for cell/ECM growth on 3D surfaces using the level set method: a bone tissue engineering case study," *Biomech. Model. Mechanobiol.*, vol. 13, no. 6, pp. 1361–1371, Nov. 2014, doi: 10.1007/s10237-014-0577-5

[44] N. G. Khouri, J. O. Bahú, C. Blanco-Llamero, P. Severino, V. O. C. Concha, and E. B. Souto, "Polylactic acid (PLA): Properties, synthesis, and biomedical applications – A review of the literature," *J. Mol. Struct.*, vol. 1309, p. 138243, Aug. 2024, doi: 10.1016/j.molstruc.2024.138243

[45] "RS PRO Coaxial connector, 50Ω Straight Flange Mount SMA Connector, jack, Coaxial". [Online]. Available: https://docs.rs-online.com/62f1/A700000007669316.pdf

[46] M. Monteagudo Honrubia, J. Matanza Domingo, F. J. Herraiz-Martínez, and R. Giannetti, "Low-Cost Electronics for Automatic Classification and Permittivity Estimation of Glycerin Solutions Using a Dielectric Resonator Sensor and Machine Learning Techniques," *Sensors*, vol. 23, no. 8, p. 3940, Apr. 2023, doi: 10.3390/s23083940

[47] P. Casacuberta, A. Ebrahimi, P. Vélez, L. Su, X. Canalias, K. Ghorbani, and F. Martín, "Sensitivity optimization in single-frequency planar microwave sensors for solid and liquid characterization and microfluidics," *IEEE Trans. Microw. Theory Techn.,* vol. 73, no. 3, pp. 1–29, Mar. 2025, doi: 10.1109/TMTT.2024.3452433

[48] M. Abdolrazzaghi, R. Genov, and G. V. Eleftheriades, "A single-frequency amplitude-modulated RFID portable backscatter surface scanner for near-field permittivity imaging," *IEEE Access,* vol. 13, pp. 1–15, 2025, doi: 10.1109/ACCESS.2025.3635387

Paris Sofokleous received the B.Sc. degree in Physics from the Aristotle University of Thessaloniki, Greece, in 2019, and the M.Sc. degree in Nanoscale Engineering from Université Claude Bernard Lyon 1, in collaboration with École Centrale de Lyon and INSA Lyon, France, in 2021. In 2022, he joined the ICAI School of Engineering and the Institute for Research in Technology (IIT) at Universidad Pontificia Comillas, where he is currently in the final stages of his Ph.D. in Modeling Systems Engineering.

His research focuses on nanotechnology, biomaterials, additive manufacturing, and electromagnetic sensing technologies. He has co-authored two scientific publications and has contributed to several international conferences. His work bridges physics, engineering, and emerging manufacturing technologies, reflecting a strong commitment to interdisciplinary research and innovation.

Eva Paz received the M.Sc. degree in Industrial Engineering with a specialization in Chemical Engineering and the M.Sc. degree in Production Engineering, as well as the Ph.D. degree in Engineering Systems Modeling. She is currently an Associate Professor with the Department of Mechanical Engineering, ICAI School of Engineering, Universidad Pontificia Comillas, Madrid, Spain, where she also coordinates the Bioengineering Area at the Institute for Research in Technology (IIT).

Her research interests focus on materials for medical applications, including biomechanical testing, mechanical characterization, additive manufacturing (3D printing), and the design of advanced materials for orthopedic surgery and bone regeneration.

Francisco Javier Herraiz-Martínez (Member, IEEE) received the M.Sc. degree in telecommunications engineering and the Ph.D. degree (Hons.) from Universidad Carlos III de Madrid, Madrid, Spain, in 2006 and 2010, respectively.

During his doctoral studies, he was a Visiting Researcher with École Polytechnique Fédérale de Lausanne (EPFL), Lausanne, Switzerland, and the University of Birmingham, Birmingham, U.K. He subsequently held a postdoctoral position with CIMITEC, Universitat Autònoma de Barcelona (UAB), Bellaterra, Spain. From 2012 to 2017, he was a Visiting Lecturer with Universidad Carlos III de Madrid. In 2017, he joined the ICAI School of Engineering and the Institute for Research in Technology (IIT), Universidad Pontificia Comillas, Madrid, Spain, where he is currently an Associate Professor.

His research interests include passive sensors and RFID systems, electromagnetic metamaterials, antennas, and microwave circuits. He has authored or co-authored over 30 journal papers and around 100 conference contributions.

Dr. Herraiz-Martínez received the Best Master Thesis Award from COIT/AEIT in 2006 and was a recipient of a Spanish Ministry of Education grant supporting his Ph.D. studies.received the M.Sc. degree in Industrial Engineering with a specialization in Chemical Engineering and the M.Sc. degree in Production Engineering, as well as the Ph.D. degree in Engineering Systems Modeling. She is currently an Associate Professor with the Department of Mechanical Engineering, ICAI School of Engineering, Universidad Pontificia Comillas, Madrid, Spain, where she also coordinates the Bioengineering Area at the Institute for Research in Technology (IIT).

Her research interests focus on materials for medical applications, including biomechanical testing, mechanical characterization, additive manufacturing (3D printing), and the design of advanced materials for orthopedic surgery and bone regeneration.